JOURNAL OF SPACECRAFT AND ROCKETS
Vol. 44, No. 2, March–April 2007

Nonlinear Longitudinal Dynamical Model of an Air-Breathing Hypersonic Vehicle

Michael A. Bolender* and David B. Doman†
U.S. Air Force Research Laboratory, Wright–Patterson Air Force Base, Ohio 45433

DOI: 10.2514/1.23370

A nonlinear, physics-based model of the longitudinal dynamics for an air-breathing hypersonic vehicle is developed. The model is derived from first principles and captures a number of complex interactions between the propulsion system, aerodynamics, and structural dynamics. Unlike conventional aircraft, air-breathing hypersonic vehicles require that the propulsion system be highly integrated into the airframe. Furthermore, full-scale hypersonic aircraft tend to have very lightweight, flexible structures that have low natural frequencies. Therefore, the first bending mode of the fuselage is important, as its deflection affects the amount of airflow entering the engine, thus influencing the performance of the propulsion system. The equations of motion for the flexible aircraft are derived using Lagrange's equations. The equations of motion capture inertial coupling effects between the pitch and normal accelerations of the aircraft and the structural dynamics. The linearized aircraft dynamics are found to be unstable and, in most cases, exhibit nonminimum phase behavior. The linearized model also indicates that there is an aeroelastic mode that has a natural frequency more than twice the frequency of the fuselage bending mode, and the short-period mode is very strongly coupled with the bending mode of the fuselage.

Nomenclature

A, B, C, D	=	constants of integration
A_d	=	diffuser area ratio
A_e	=	exit area
$A_{f,k}$	=	amplitude of kth mode shape
A_i	=	inlet area
A_n	=	exit nozzle area ratio
A_s	=	spill area
A_0	=	capture area
A_1	=	total capture area
a, b, c	=	polynomial coefficients
c_p	=	specific heat
D	=	drag
$\boldsymbol{d}$	=	displacement vector of a mass element relative to its undeformed location
E	=	Young's modulus
$\boldsymbol{e}$	=	unit vector in the body-fixed frame
$F_{x,()}$	=	body-force component in x direction acting on fuselage
$F_{z,()}$	=	body-force component in z direction acting on fuselage
f	=	fuel–air ratio
f_{st}	=	stoichiometric fuel–air ratio
g	=	acceleration due to gravity
H_f	=	fuel lower heating value
h	=	altitude
h_i	=	inlet height
h_{t_2}	=	total enthalpy at the combustor inlet
h_{t_3}	=	total enthalpy at the combustor exit
I	=	moment of inertia
L	=	lift
$L_{()}$	=	length of subscripted component
M	=	Mach number (when subscripted with a number), pitching moment
m	=	mass
$\hat{m}$	=	mass distribution
$\dot{m}_a$	=	mass flow of air
$\dot{m}_f$	=	mass flow of fuel
$\boldsymbol{n}$	=	unit vector in the inertial frame
$P_j(t)$	=	concentrated load
p	=	pressure
$p_{cs,\ell}$	=	pressure on bottom surface of the elevator
$p_{cs,u}$	=	pressure on upper surface of the elevator
$p(x, t)$	=	distributed load
Q	=	generalized force, pitching rate
q	=	generalized coordinate
$\mathcal{R}$	=	rotation matrix
$\boldsymbol{r}_{b/a}$	=	position vector of point B relative to point A
$\boldsymbol{r}_0$	=	inertial position vector of the center of gravity
S_{cs}	=	elevator area
s	=	Laplace variable
s_a	=	distance along aftbody panel
$\mathcal{T}$	=	engine thrust
$\mathcal{L}$	=	Lagrangian
$\mathcal{J}$	=	kinetic energy
$T_{()}$	=	temperature at subscripted station
t	=	time
U	=	velocity along x body axis
u	=	$\boldsymbol{e}_1$ coordinate of mass element dm in body frame
$\mathcal{V}$	=	potential energy
V_e	=	exhaust exit velocity
V_t	=	true airspeed
V_∞	=	velocity of the freestream
W	=	velocity along z body axis
$\mathcal{W}$	=	work
w	=	$\boldsymbol{e}_3$ coordinate of mass element dm in body frame
$w(x, t)$	=	structural displacement
X	=	$\boldsymbol{n}_1$ coordinate of aircraft c.g. measured in inertial frame
x	=	inertial position of aircraft c.g. written in the body-axis coordinates
x	=	spatial coordinate
$\bar{x}$	=	center of gravity
$x_{()}$	=	x coordinate relative to the c.g.
Z	=	$\boldsymbol{n}_3$ coordinate of aircraft c.g. measured in inertial frame, force in z stability axis

Presented as Paper 6255 at the AIAA Guidance, Navigation, and Control Conference and Exhibit, San Francisco California, 15–18 August 2005; received 22 February 2006; revision received 13 June 2006; accepted for publication 14 July 2006.

*Aerospace Engineer. Senior Member AIAA.
†Senior Aerospace Engineer. Associate Fellow AIAA.

z = inertial position of aircraft c.g. written in body-axis coordinates
$z_{()}$ = z coordinate relative to the c.g.
$z_{\mathcal{T}}$ = thrust line-of-action offset from the c.g.
α = angle of attack
γ = ratio of specific heats, flight-path angle
ΔT_{t_c} = change in total temperature in the combustor
δ = flow turn angle, variation, Dirac delta
δ_{cs} = elevator deflection
$\delta/\delta t$ = time derivative relative to a moving frame
η_c = combustor efficiency
η_k = kth generalized modal coordinate
θ = pitch attitude
θ_s = oblique shock angle, rad
$\lambda_{z,i}$ = inertial coupling parameter
ν_1 = angle through which a flow at Mach 1 is expanded to achieve the freestream Mach
ν_2 = total angle through which the flow is expanded
$\boldsymbol{\rho}$ = position of a mass element relative to the c.g. in the rigid body
$\sigma_{z,i}$ = inertial coupling parameter
$\tau_{1,\ell}$ = lower forebody turn angle with respect to x_B axis
$\tau_{1,u}$ = upper forebody turn angle with respect to x_B axis
τ_2 = aftbody vertex angle
Φ = equivalence ratio
$\phi(x)$ = structural mode shape
$\psi_{xz,i}$ = inertial coupling parameter
$\boldsymbol{\omega}$ = angular velocity vector
ω = natural frequency

Subscripts

a = aftbody panel, aft beam
cs = elevator
f = forebody, forward beam
n = nacelle
q = stability derivative with respect to pitch rate
t = stagnation
u = upper surface
α = stability derivative with respect to angle of attack
$\dot{\alpha}$ = stability derivative with respect to time rate-of-change of angle of attack
1,2,... = static conditions at a station behind shock/expansion fan
∞ = freestream properties

Superscripts

$\dot{()}$ = derivative with respect to time

I. Introduction

AIR-BREATHING hypersonic aircraft are seen as a possible solution to making access to space routine and affordable. Research into air-breathing hypersonics began during the 1960s and continued through the 1990s with the National Aerospace Plane. In spite of this long period of research, it is widely recognized that the development of a full-scale operational vehicle will require major advances in propulsion and materials technology as well as more mature multidisciplinary modeling and design tools. After the cancellation of the National Aerospace Plane in the early 1990s, there have been a few programs that were intended to demonstrate the feasibility of component technologies needed to achieve sustained hypersonic flight. The most recent example has been NASA's successful flight tests of the scramjet-powered X-43A, a subscale technology demonstrator that flew in 2004 and 2005.

The design of air-breathing hypersonic vehicles typically has a tightly integrated airframe and scramjet propulsion system. The design is such that the forward fuselage of the aircraft creates a bow shock that acts as a compression system for the scramjet engine. The pressure distribution on the forebody also produces lift and a nose-up pitching moment. Downstream of the scramjet engine, the aircraft is shaped such that there is an external expansion of the exhaust gases. The pressure on the aftbody is a function of the pressure of the exhaust gas as it exits the scramjet engine and this pressure contributes to the lift of the vehicle, partially offsets the drag, and partially balances the vehicle with a nose-down pitching moment. With the engine below the center of gravity, the thrust produces a nose-up pitching moment that must be balanced by the aerodynamics and control surfaces. The structural modes for this class of vehicle also play an important role. The vibrating, forward fuselage effectively changes the pressure distribution over the forebody of the aircraft, because it changes the apparent turn angle of the flow. The resulting changes in the pressure distribution over the aircraft are realized downstream not only as thrust perturbations, but as lift, drag, and pitching moment perturbations as well.

In the literature, there have been several papers that discuss the challenges associated with the dynamics and control of air-breathing hypersonic vehicles (HSVs) [1,2]. The first attempt at a comprehensive analytical model of the longitudinal dynamics of an HSV was undertaken by Chavez and Schmidt [3]. The use of Newtonian impact theory allowed for a straightforward determination of the expressions for the pressures acting on the vehicle. The pressures were dependent upon vehicle Mach number, freestream pressure, angle of attack, and the vehicle geometry. These expressions were then manipulated to give the total aerodynamic forces on the vehicle. The resulting equations were then linearized to give analytical expressions for the stability and control derivatives. Ultimately, requirements and control laws for the Chavez–Schmidt HSV were synthesized [1,4].

Von Eggers Rudd and Pines [5] applied a computational fluid dynamics code written to optimize the L/D of a caret-wing-wedge hypersonic wave rider. The code was then used to study the propulsion–airframe integration and to estimate the stability and control derivatives. These stability and control derivatives were then compared with those estimated using hypersonic piston theory. The vehicle design included a translating engine cowl to maintain a shock-on-lip condition. An LQR control design was performed using the stability and control derivatives derived using both approaches. The results showed that piston theory was not able to accurately determine the stability derivatives (with the exception being the lift curve slope). The inaccuracy is caused by hypersonic piston theory not being applicable to the engine flow, because the Mach numbers within the engine are not hypersonic. As a result, the controller designed using the piston theory derived stability and control derivatives was unable to stabilize a nonlinear 3DOF simulation whose aerodynamic characteristics were computed using a CFD code.

A model of a canard-configured, generic winged-cone configuration that is intended to be representative of a single-stage-to-orbit accelerator vehicle is given in [6]. The stability and control derivatives were estimated using a subsonic–supersonic panel code and a hypersonic local surface inclination method.

Finally, the MAVRIC hypervelocity vehicle was a two-stage-to-orbit vehicle with a scramjet-powered second stage [7]. The configuration chosen for the second stage was a double delta wing with typical scramjet integration into the airframe. The supersonic–hypersonic arbitrary body program was used to generate the aerodynamic model. The first two structural modes for the longitudinal and lateral directional axes were also modeled. However, thrust perturbations due to mass flow variation and pressure changes at the inlet were not modeled, but incremental changes to the aerodynamics were considered.

In this paper, we present a model that captures the structural, aerodynamic, and propulsion system coupling inherent in a scramjet-powered vehicle. The approach taken here relaxes some of assumptions that were built into the model of Chavez and Schmidt [3] in order to address the influence of additional couplings that were expected to exist [2] at the time, but whose effects on vehicle stability and control were uncertain.

Two additional effects were considered in this dynamic model that were not considered in the references cited previously. The first effect

considered is the on-design and off-design propulsion system performance resulting from an oscillating bow shock. To include the effects of inlet mass flow spillage due to an oscillating bow shock, we make use of oblique shock and Prandtl–Meyer expansion theory rather than Newtonian impact theory, which was employed in [3]. Using this approach, we compute the location of the bow shock relative to the inlet lip and calculate the change in forces and moments due to changes in the engine inlet and exit pressures. The model captures changes in bow shock location and the forebody pressure distribution resulting from changes in angle of attack and structural flexibility.

The second effect we considered is the presence of coupling between the rigid-body accelerations and flexible body dynamics. For any flexible aircraft, the forces and moments are dependent upon the structural deflection, as this alters the pressure distribution on the vehicle; therefore, a model of the structural dynamics is necessary in order to account for these effects. The incorporation of the effects of the rigid-body vertical translation rotational effects on the fuselage dynamics is a direct result of the structural model that we chose. We chose this structural model because it gives a simple, first-order approximation of the fuselage vibration. Early in the design phase, a detailed structural vibration analysis is not available to implement in the flight dynamics model; therefore, a simple model was developed that captured the gross behavior of the fuselage under loading. In contrast, the model developed in [3] implemented a vibrational model that was derived from a finite-element analysis of a full-scale hypersonic vehicle. The result of finite-element analysis was a model whose structural modes and rigid-body modes were decoupled.

The result is a representative model of the longitudinal dynamics of an air-breathing hypersonic vehicle that captures many of the effects of the diverse physical phenomena that present challenges to flight control designers. The form of the model is suitable for use in configuration trade: studies early in the design process where designers are interested in developing a configuration that is amenable to feedback control.

II. Aerodynamic and Propulsive Force Determination

The goal of this research is to extend the work done previously by Chavez and Schmidt [3]. One difference between this effort and that in [3] is that we apply oblique shock and Prandtl–Meyer theory instead of Newtonian impact theory to calculate the surface pressures and to determine the effect of mass flow spillage on the forces and moments as the bow shock oscillates due to flexible body effects. The primary difference between the two theories is that Newtonian impact theory is more suited to calculating the pressure distribution on blunt shapes, as Newtonian impact theory underestimates the pressure when used for two-dimensional geometries such as wedges [8]. Further justification for our use of 2-D gas dynamics is that our vehicle will employ a translating cowl door to maintain a shock-on-lip condition for off-design flight conditions in order to maximize the mass flow through the engine; however, the translating door is treated as a slowly moving surface that accounts for changes in angle of attack and Mach number and not necessarily flexibility effects. To position the cowl door, one must know the angle that the oblique shock makes relative to the freestream. Newtonian impact theory assumes that the oblique bow shock lies very close to the body as $M_\infty \to \infty$, in fact, it can be shown that in the limit, $\theta_s = 1.2\delta$. In actuality, the angle that the oblique shock makes relative to the freestream is not indicative of its actual angle at the lower end of the hypersonic speed range. Therefore, we are relegated to using oblique shock theory for our pressure calculation on the lower forebody in order to determine the angle of the oblique shock relative to the freestream.

The vehicle geometry that was chosen for this work is shown in Fig. 1. It is assumed that the vehicle shown has unity depth into the paper and that air behaves as if it is a perfect gas (i.e., the ratio of specific heats is a constant).

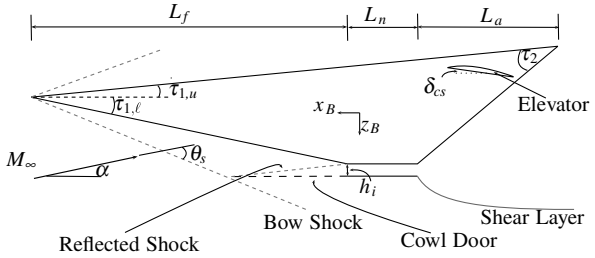

Fig. 1 Hypersonic air-breathing vehicle geometry.

A. Forebody and Upper-Surface Pressures

The pressure on the forebody is determined by either oblique shock theory or Prandtl–Meyer flow and is dependent upon the angle of attack and the amount of structural bending. When the angle of attack is greater than the angle $-\tau_{1,\ell}$, the flow behaves as if it is flowing over a concave corner; therefore, an oblique shock occurs ahead of the lower forebody. The shock angle with respect to the horizontal (in this case, taken to be the direction of the oncoming freestream flow), is a function of angle of attack and $\tau_{1,\ell}$. The shock angle is calculated by solving the following polynomial for $\sin^2\theta_s$ (see [9]):

$$\sin^6\theta_s + b\sin^4\theta_s + c\sin^2\theta_s + d = 0 \tag{1a}$$

$$b = -\frac{M_\infty^2 + 2}{M_\infty^2} - \gamma\sin^2\delta \tag{1b}$$

$$c = \frac{2M_\infty^2 + 1}{M_\infty^4} + \left[\frac{(\gamma+1)^2}{4} + \frac{\gamma - 1}{M_\infty^2}\right]\sin^2\delta \tag{1c}$$

$$d = -\frac{\cos^2\delta}{M_\infty^4} \tag{1d}$$

The angle of the oblique shock is given by the second root of Eq. (1a), as this particular wave angle corresponds to the weak shock solution. The smallest of the three roots corresponds to a decrease in entropy. Because this solution is not physically realizable, it is discarded. The largest root is the strong shock solution and is not of interest, as the back pressures are not strong enough to support this solution.

Once the shock angle is determined, the pressure, temperature, and Mach number behind the oblique shock can be determined from the following relations [9]:

$$\frac{p_1}{p_\infty} = \frac{7M_\infty^2\sin^2\theta_s - 1}{6} \tag{2}$$

$$\frac{T_1}{T_\infty} = \frac{\left(7M_\infty^2\sin^2\theta_s - 1\right)\left(M_\infty^2\sin^2\theta_s + 5\right)}{36M_\infty^2\sin^2\theta_s} \tag{3}$$

$$M_1^2\sin^2(\theta_s - \delta) = \frac{M_\infty^2\sin^2\theta_s + 5}{7M_\infty^2\sin^2\theta_s - 1} \tag{4}$$

On the other hand, in the cases where we have flow over a convex corner, we will have a Prandtl–Meyer expansion [10]. The process for calculating the new Mach number after the expansion requires that one first determine the angle ν_1.

$$\nu_1 = \sqrt{\frac{\gamma+1}{\gamma-1}}\tan^{-1}\sqrt{\frac{\gamma-1}{\gamma+1}\left(M_1^2-1\right)} - \tan^{-1}\sqrt{M_1^2-1} \tag{5}$$

To determine the resulting Mach number after the expansion M_1, the following equation must be solved numerically:

$$f(M_1) = \sqrt{\frac{\gamma+1}{\gamma-1}}\tan^{-1}\sqrt{\frac{\gamma-1}{\gamma+1}\left(M_1^2-1\right)} - \tan\sqrt{M_1^2-1} - \nu_2 \tag{6}$$

Once the solution to Eq. (6) is determined, the flow properties after the expansion are found from the thermodynamic relations for isentropic flow [9]:

$$\frac{p_1}{p_\infty} = \left[\frac{1+[(\gamma-1)/2]M_{1\infty}^2}{1+[(\gamma-1)/2]M_1^2}\right]^{\gamma/(\gamma-1)} \tag{7}$$

$$\frac{T_1}{T_\infty} = \left[\frac{1+[(\gamma-1)/2]M_\infty^2}{1+[(\gamma-1)/2]M_1^2}\right] \tag{8}$$

Prandtl–Meyer theory predicts that as $M_1 \to \infty$, the maximum angle through which the flow can be expanded is 130.4 deg. This implies that there are cases where the numerical solution of Eq. (6) will not converge. For purposes of simulation, this upper bound on the expansion angle imposes limits on the angle of attack and on the control surface deflection. In the latter case, the control surface deflection limit may be less than that imposed by the actuator.

Once the downstream pressures are calculated according to either oblique shock theory or Prandtl–Meyer expansion flow theory, we can determine the aerodynamic forces acting on the vehicle. From Fig. 1, the pressure on the lower forebody can be resolved into its x and z body-axis components:

$$F_{x,f} = -p_f L_f \tan\tau_{1\ell} \tag{9}$$

$$F_{z,f} = -p_f L_f \tag{10}$$

Note that L_f is measured parallel to the body x axis. The pitching moment due to the lower forebody aerodynamic forces is

$$M_f = z_f F_{x,f} - x_f F_{z,f} \tag{11}$$

The aerodynamic center of the lower forebody occurs at the midpoint of the panel, (x_f, z_f), because the pressure distribution on the lower forebody is uniform behind the oblique shock wave.

Likewise, the pressures on the upper surface of the aircraft give the following body-axes forces and pitching moment:

$$F_{x,u} = -p_u L_u \tan\tau_{1u} \tag{12}$$

$$F_{z,u} = p_u L_u \tag{13}$$

$$M_u = z_u F_{x,u} - x_u F_{z,u} \tag{14}$$

The coordinates of the center of the upper-surface panel relative to the center of mass are given by (x_u, z_u).

B. Scramjet Model

In the hypersonic flight regime, to produce the thrust necessary to maintain sustained flight, one is limited to one of two possible propulsion systems: rocket propulsion or a supersonic combustion ramjet engine (scramjet). Advantages of ramjet engines are their simplicity, as no rotating turbomachinery is necessary, and their efficient operation at supersonic speeds. The disadvantages are they are not self-starting and are not very efficient at subsonic speeds. A conventional ramjet slows the flow through a diffuser, and so the combustor operates at pressures and temperatures that are near stagnation conditions. However, as Mach number increases to approximately Mach 5, the losses and the associated heating that are experienced when reducing the flow to subsonic Mach numbers become significant. Therefore, the scramjet becomes the more viable option for air-breathing propulsion above Mach 5. Another advantage of the ramjet engine over the rocket engine is that it offers an opportunity for increased payload. Unlike the rocket engine, which requires that both the oxidizer and the fuel be carried onboard the vehicle, the scramjet only requires that the aircraft carry the fuel. Therefore, the volume that is dedicated to carrying an oxidizer for the rocket can now be used for payload. However, one downside of the scramjet is that it is only operable from Mach 5–16 [11]. To overcome this, one concept that has been proposed is the rocket-based combined-cycle propulsion system that marries the rocket, ramjet, and scramjet cycles into a single propulsion system [12]. This propulsion system accommodates all phases of flight from subsonic to supersonic to hypersonic to orbital.

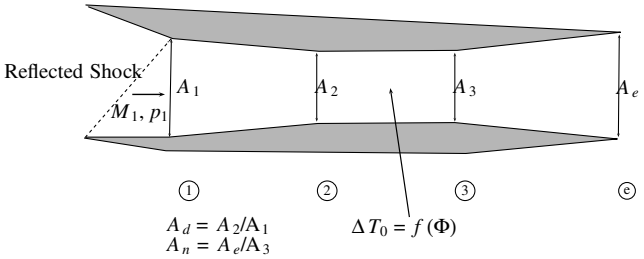

Fig. 2 Scramjet cross section.

The scramjet used for this model is shown in Fig. 2 and is similar to that used by Chavez and Schmidt [3]. The conditions given at the engine inlet (station 1) are primarily determined by the Mach number and angle of attack at which the aircraft is flying. These parameters determine, in part, the properties of the bow shock. The flow through the diffuser is assumed to be isentropic (i.e., without loss). The two control variables that determine the thrust setting are the diffuser area ratio and the equivalence ratio. The equivalence ratio effectively determines the change in total temperature that results from the combustion process. Choosing Φ as a control parameter is the same as controlling the fuel flow, because we can calculate how much air is captured by the propulsion system. This avoids us from having to make a priori assumptions regarding the fuel schedule and the parameters used for scheduling. Controlling A_d allows one to modulate the Mach number and the static pressure of the air entering into the combustion chamber. Ideally, the air remains supersonic to avoid significant ram drag penalties. Because the air entering the combustor is supersonic, the heat release due to fuel combustion *reduces* the Mach number of the airstream that is passing through the engine. Care must be taken to ensure that the amount of heat added does not thermally choke the combustor flow.

In the diffuser, we apply the continuity equation (conservation of mass) to determine the Mach number at the diffuser exit/combustor inlet (station 2) given the diffuser inlet Mach:

$$\frac{\left\{1+[(\gamma-1)/2]M_2^2\right\}^{(\gamma+1)/(\gamma-1)}}{M_2^2} = A_d^2\frac{\left\{1+[(\gamma-1)/2]M_1^2\right\}^{(\gamma+1)/(\gamma-1)}}{M_1^2} \tag{15}$$

The pressure and temperature at station 2 are determined by Eqs. (7) and (8).

The combustor is modeled as a constant-area, frictionless duct with heat addition. The Mach number at the combustor exit (station 3) is given by

Table 1 Properties of common scramjet fuels

Fuel	f_{st}	H_f, BTU/lbm	c_p, BTU/(lbm °R)
LH2	0.0291	51,500	0.24
JP-8	0.0664	19,100	0.54

$$\frac{M_3^2\left[1+\frac{1}{2}(\gamma-1)M_3^2\right]}{\left(\gamma M_3^2+1\right)^2}=\frac{M_2^2\left[1+\frac{1}{2}(\gamma-1)M_2^2\right]}{\left(\gamma M_2^2+1\right)^2}+\frac{M_2^2}{\left(\gamma M_2^2+1\right)^2}\frac{\Delta T_c}{T_2} \tag{16}$$

The pressure and temperature at the combustor exit are

$$p_3 = p_2\frac{1+\gamma M_2^2}{1+\gamma M_3^2} \tag{17}$$

$$T_3 = \frac{M_3^2}{M_2^2}\frac{\left(1+\gamma M_2^2\right)^2}{\left(1+\gamma M_1^2\right)^2} \tag{18}$$

The change in total temperature in Eq. (16) is due to the burning of fuel (either liquid hydrogen (LH2) or a hydrocarbon-based fuel such as JP-8). Engine thrust is strongly dependent upon the fuel-to-air ratio ($f = \dot{m}_f/\dot{m}_a$) in the combustor. Typically, the fuel-to-air ratio is normalized by the stoichiometric fuel-to-air ratio, and the fuel equivalence ratio is used as a control input to the engine instead of the change in total temperature across the combustor. Numerically, this approach avoids some of the scaling problems associated with using the change in temperature as a control input. The fuel equivalence ratio is defined as $\Phi = f/f_{st}$. If we examine the enthalpy flux for the control volume defined from the combustor inlet to the combustor exit (between stations 2 and 3 in Fig. 2), we have [13]

$$\eta_c \dot{m}_f H_f = \dot{m}_a(h_{t_3} - h_{t_2}) + \dot{m}_f h_{t_3} \tag{19}$$

Values of f_{st} and H_f for LH2 and a hydrocarbon fuel are given in Table 1 and are taken from Heiser and Pratt [11], whereas the values for c_p are taken from [14]. It is assumed that the combustion efficiency is $\eta_c = 0.9$. Substituting for the total enthalpy ($h_t = c_p T_t$) at the combustor inlet and exit planes and using the definition for f, we are able to solve for the ratio of total temperature at the combustor exit to the total temperature at the combustor inlet:

$$\frac{T_{t3}}{T_{t2}} = \frac{1+H_f\eta_c f_{st}\Phi/(c_p T_{t2})}{1+f_{st}\Phi} \tag{20}$$

Once we have computed the ratio T_{t_3}/T_{t_2}, we can easily compute $\Delta T_{t_c} = T_{t_3} - T_{t_2}$ for inclusion into Eq. (16). At this time it should be noted that the equivalence ratio maps linearly to the change in total temperature in the combustor, which, in turn, maps linearly to the thrust (see Fig. 3). In actuality, one expects to see a decrease in thrust for some value of ϕ that is slightly above unity. Because our particular combustion model does not capture the finite-rate chemistry that occurs in the combustion process, the model is only physically meaningful where the thrust is a linear function of the equivalence ratio.

The flow, upon leaving the combustor, enters a diverging, isentropic nozzle that will ultimately increase the exit Mach number. The exit nozzle area ratio is assumed to be fixed. The exit Mach number is given by

$$\frac{\left\{1+[(\gamma-1)/2]M_e^2\right\}^{(\gamma+1/\gamma-1)}}{M_e^2} = A_n^2\frac{\left\{1+[(\gamma-1)/2]M_3^2\right\}^{(\gamma+1/\gamma-1)}}{M_3^2} \tag{21}$$

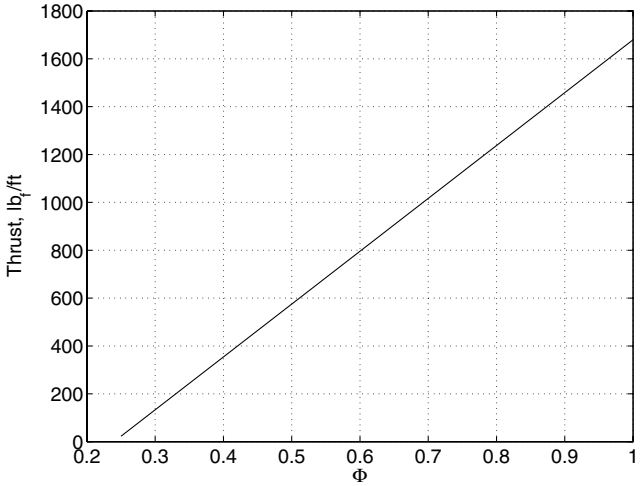

Fig. 3 Thrust vs equivalence ratio at Mach 10, 110,000 ft, fuel is LH2, and the geometry is as in Appendix A.

and the pressure and temperature at the exit plane are given by Eqs. (7) and (8).

The thrust is calculated by applying the momentum theorem from fluid mechanics to a control volume that encloses the scramjet engine. The thrust is given by

$$\mathcal{T} = \dot{m}_a(V_e - V_\infty) + (p_e - p_\infty)A_e - (p_1 - p_\infty)A_i \tag{22}$$

It has been assumed that the mass flow of the fuel is negligible when compared with the mass flow of air.

An important parameter in the thrust equation (22) is the term for the mass flow of air. The amount of mass flow captured by the engine inlet is a function of the shock angle, as shown in Fig. 4. Typically, the aircraft geometry is designed such that the bow shock impinges upon the engine inlet lip at the design cruise condition. This will result in maximum mass flow through the engine module. At off-design conditions where the bow shock no longer impinges on the lip (cruise Mach less than the design Mach at the same angle of attack), there will be mass flow spillage, as the shock will be positioned in front of the cowl lip. For the present discussion, we assume that there exists a translating cowl lip that can be positioned instantaneously to be coincident with the bow shock; however, we will relax this assumption in the subsequent section. By positioning the cowl lip in such a manner, we can optimize the mass flow through the engine for any off-design flight condition. However, the lift, drag, and pitching moment are now affected by the length of the cowl lip. When the cowl lip intersects the shock, a second oblique shock occurs under the engine nacelle for positive angles of attack. For negative angles of attack, there is a Prandtl–Meyer expansion fan that turns the flow parallel to the nacelle. The pressure can be calculated using the methods given in the previous section. The only contribution is to the z axis body force, as it is assumed that the engine cowl is parallel to x body axis.

$$F_{z,n} = -p_n L_n \tag{23}$$

The nacelle length L_n is the sum of the nominal nacelle length with the door completely retracted, L_{n0}, and the length of the translating lip $L_n = L_{n0} + L_{\text{door}}$. From Fig. 4, the length of the cowl door required to intersect the shock when the vehicle is at an angle of

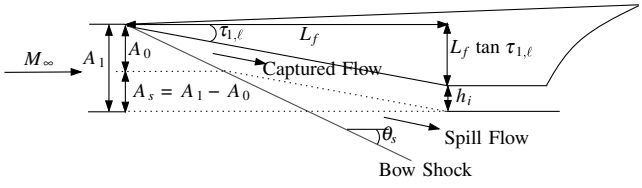

Fig. 4 Capture area/mass flow spillage.

attack of α is

$$L_{\text{door}} = L_1 - (L_1 \tan \tau_{1\ell} + h_i) \cot(\theta_s - \alpha) \tag{24}$$

where h_i is as defined in Fig. 1. The pitching moment created by $F_{z,n}$ is

$$M_n = -F_{z,n}\left[x_{n0} + \tfrac{1}{2}(L_{\text{door}} - L_{n0})\right] \tag{25}$$

1. Mass Flow Spillage Effects

In this section, we discuss the effects of mass flow spillage on the thrust and the system dynamics. Deflection of the forebody due to aerodynamic forces may be problematic if the pressure and mass flow changes that occur significantly change the thrust, lift, and pitching moment. Furthermore, changes in the stability and control derivatives due to the structural dynamics could possibly have adverse effects on the pole and zero locations, which, in turn, could degrade the gain and phase margins of an inner-loop control system. If mass flow spillage effects are not negligible, then some sort of active control device may be necessary in order to regulate the mass flow of air into the engine. For example, in the preceding section, we have assumed the presence of a translating cowl door during the development of the forces and moments on the vehicle that were presented previously. In this case, the translating cowl door was used to maintain a shock-on-lip condition and thus maximize the airflow through the engine. This is an idealized situation, because we assume that there is a mechanism in place to retract and extend the door and that aerodynamic heating due to shock impingement, which is significant, is neglected. The analysis that follows provides insight into the sensitivity of the thrust and the open-loop dynamics due to changes in the flow turn angle.

Consider the case where the vehicle is in straight and level flight and is flying at a Mach number lower than the design Mach number, which results in mass flow spillage, because the oblique shock that turns the flow parallel to the lower forebody is not attached to the engine cowl. This situation is shown in Fig. 4.

For a fixed Mach number and wedge angle, the mass flow capture area is a function of angle of attack only. The geometry of the capture area of a scramjet engine is given in Fig. 4. It can be shown using elementary trigonometry that the ratio of capture area to inlet area can be given by

$$\frac{A_0}{h_i} = \frac{\sin\theta \cos\delta}{\sin(\theta - \alpha - \delta)} \tag{26}$$

Recall that the shock angle is found by solving Eq. (1a).

The total capture area is denoted in Fig. 4 by A_1. The total capture area is given by the relation

$$A_1 = [L_f(\tan\alpha + \tan\delta) + h_i]\cos\alpha \tag{27}$$

or, equivalently, the area ratio is

$$\frac{A_1}{h_i} = \frac{L_f}{h_i}[\sin\alpha + \tan\delta\cos\alpha] + \cos\alpha \tag{28}$$

The spill flow area is simply the difference between the total area and the capture area and is shown in Fig. 4 as A_s. Representative curves for each area are shown in Fig. 5.

We see in Fig. 5 that the amount of mass flow that is spilled when the shock does not intersect the cowl lip increases with increasing angle of attack. However, this potential problem is mitigated, because both the capture area and the total area are increasing over the angle of attack range plotted here. The total area increases linearly with angle of attack, but the capture area does not. The capture area behaves linearly up until a 4-deg angle of attack before its slope becomes shallower due to the sine term in the denominator. What these curves indicate is that potential adverse mass flow spillage effects, which increase with angle of attack, are largely offset, because the captured mass flow also increases with angle of attack.

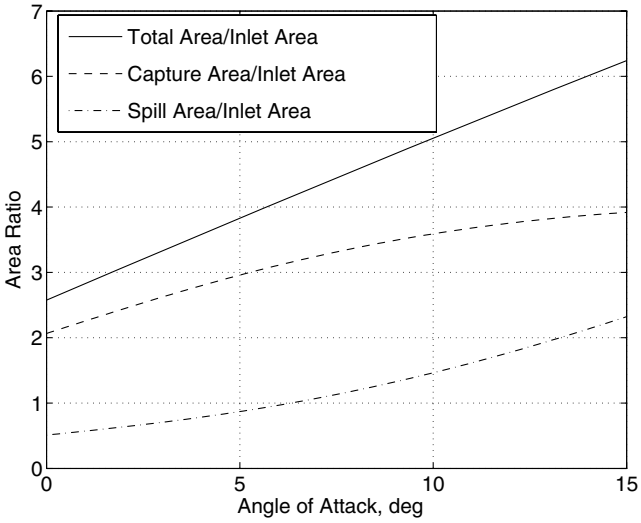

Fig. 5 Area ratio as a function of angle of attack for a fixed Mach number and wedge angle.

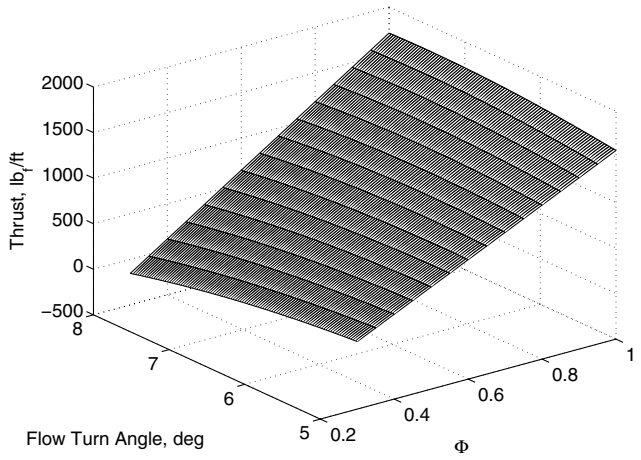

Fig. 6 Thrust as a function of equivalence ratio and flow turn angle at Mach 10, 110,000 ft, fuel is LH2, and the geometry is as in Appendix A.

To further quantify the effects of varying mass flow into the engine, we will look at sensitivities in thrust due to perturbations in the flow turn angle. This is equivalent to looking at the effects of small structural deflections or even those effects resulting from perturbing the angle of attack.

We will begin by looking at the thrust map (Fig. 6) for a representative HSV that contains a single precompression ramp. We consider a fixed Mach number and hold the angle of attack at 0 deg. The thrust appears to vary linearly with equivalence ratio and quadratically with the flow turn angle, with the equivalence ratio having a more significant effect on the thrust level than the flow turn angle.

The thrust sensitivity to changes in the flow turn angle is given in Fig. 7. Figure 7 shows that at higher equivalence ratios, the thrust is not as sensitive to changes in the flow turn angle as compared with lower equivalence ratios. This can be attributed to the fact that increasing the flow turn angle will increase the pressure at the inlet, thus increasing the pressure throughout the scramjet. As Φ increases, the Mach number in the combustion chamber decreases, causing the static pressure to rise. When this flow is expanded through the diverging nozzle, the exit pressure decreases and the exit Mach increases.

Let us once again examine the thrust equation as given in Eq. (22). The first term in Eq. (22), which corresponds to the momentum flux, increases with increasing Φ. At the lower Φ values in Fig. 7, the momentum flux is approximately the same magnitude as the pressure

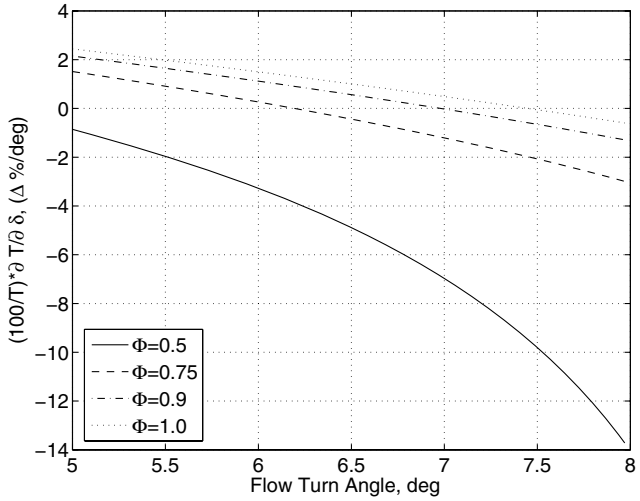

Fig. 7 Sensitivity of thrust to changes in flow turn angle; fuel is LH2, the geometry is as in Appendix A.

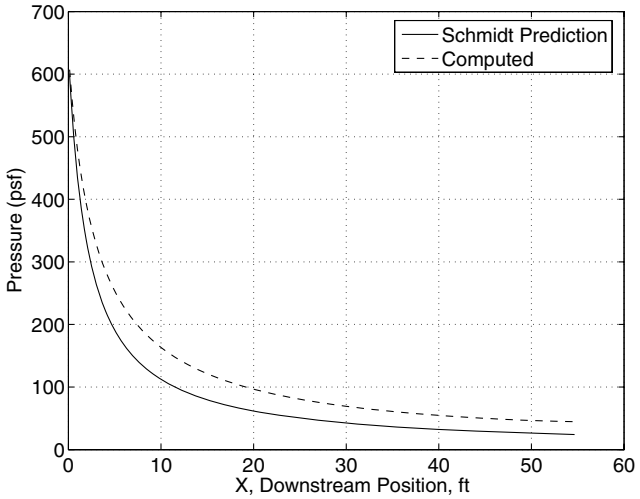

Fig. 8 Comparison of approximate and exact pressure acting on the aftbody of the HSV.

drag on the inlet face. Therefore, at lower Φ values, the thrust will be more sensitive to changes in pressure due to changes in the flow turn angle. As the flow turn angle increases, the pressure increases at the inlet face, increasing the inlet pressure drag. To optimize the pressure at the engine inlet, a series of compression ramps is used to generate oblique shock waves that incrementally increase the static air pressure and turn the oncoming airflow axial to the engine. Hypersonic aircraft tend to have initial flow turn angles on the order of 6–8 deg, and so the thrust sensitivity in this range is of interest. Furthermore, an operational scramjet will probably run closer to a stoichiometric condition than what we considered here, thus reducing the sensitivity further as the upper curves continue to flatten out. For example, the model on which this analysis is based trims in level, unaccelerating flight at $\Phi = 0.4$ at Mach 8, 85,000 ft and $\Phi = 1.03$ at Mach 10, 110,000 ft. Again, note that the thrust is a linear function in Φ, due to our model. Therefore, we do not consider the thrust perturbations due to changes in flow turn angle that result from either the structural dynamics or perturbations in angle of attack due to turbulence and unmodeled dynamics to be a concern with regards to the controllability of the vehicle.

A sensitivity analysis of the poles and transmission zeros was performed and showed that the migration of the poles and zeros due to changes in the flow turn angle δ are not significant (less than 1%). This analysis assumed only single compression ramp and no mass or moment of inertia changes due to the change in the shape of the forebody. Therefore, because the changes in the system dynamics that occur are minimal, the control system stability and robustness is unlikely to be adversely impacted by perturbations in the flow turn angle that result from structural bending.

2. Engine Inlet Turning Force

The airflow, after passing through the oblique shock, is parallel to the forebody; therefore, it must be turned parallel to the engine centerline. As a result, the force imparted by the air on the aircraft is

$$F_{x,\text{inlet}} = \gamma M_1^2 p_1 [1 - \cos(\tau_{1,\ell} + \alpha)] h_i \tag{29}$$

$$F_{z,\text{inlet}} = \gamma M_1^2 p_1 \sin(\tau_{1,\ell} + \alpha) h_i \tag{30}$$

$$M_{\text{inlet}} = z_{\text{inlet}} F_{x,\text{inlet}} - x_{\text{inlet}} F_{z,\text{inlet}} \tag{31}$$

The mechanism for turning the flow axial to the engine is a second oblique shock, and there will be a resulting rise in static pressure and temperature and a decrease in Mach number as the flow crosses this shock. The new pressures and temperatures are calculated using the expressions given previously.

C. Aftbody Pressure

The pressure acting on the aftbody of the vehicle is due to the external expansion of the exhaust from the scramjet engine. The aftbody forms the upper part of a nozzle,, whereas the shear layer that results from the interaction of the exhaust plume with the freestream flow forms the lower surface. The pressure distribution along the aftbody is then a function of the position of the shear layer. The shear layer is formed where the pressure in the plume is balanced by the freestream pressure. A reasonable approximation for the pressure at any point on the aftbody is given by Chavez and Schmidt [3]

$$p_a = \frac{p_e}{1 + s_a / L_a (p_e / p_\infty - 1)} \tag{32}$$

as shown in Fig. 1.

A comparison of the approximate pressure, as given by Eq. (32), to the pressure calculated after determining the exact position of the shear layer is given in Fig. 8. The exact position of the shear layer was calculated by approximating the plume by a series of panels. Given the ambient atmospheric pressure, the exit pressure from the engine internal nozzle and the angle of the expansion ramp, the location of the shear layer was calculated by balancing the atmospheric pressure with the pressure internal to the exhaust plume. It is readily evident that the approximation is of sufficient accuracy to model the aftbody pressure. The advantage of using Eq. (32) is the computational efficiency that it affords, as the determination of the shear layer position requires a rather complicated algorithm.

The aftbody pressure makes a contribution to the lift and also acts to offset the drag of the forebody. The x and z body-axis forces are

$$F_{x,a} = p_\infty L_a \frac{p_e}{p_\infty} \frac{\ell n\, p_e / p_\infty}{(p_e / p_\infty) - 1} \tan(\tau_2 + \tau_{1,u}) \tag{33}$$

$$F_{z,a} = -p_\infty L_a \frac{p_e}{p_\infty} \frac{\ell n\, p_e / p_\infty}{(p_e / p_\infty) - 1} \tag{34}$$

The pitching moment due to these forces is assumed to act on the aftbody panel at the point where the mean value of the pressure distribution occurs: $\bar{p}_a = \int_0^{L_a} p_a(x)\, dx / L_a$.

$$M_a = z_a F_{x,a} - x_a F_{z,a} \tag{35}$$

D. Control Surface Model

As shown in Fig. 1, there is a control surface available that is used to control the pitching moment acting on the aircraft. The control surface is modeled as a flat plate that is hinged at its midchord point so that the entire surface deflects. This is consistent with the designs of

both the X-43 and NASP, where the wing tips were deflected for pitch control. The pressures on the upper and lower surfaces of the elevator are determined by the incidence of the control surface with the flow. The incidence angle is a function of the angle of attack, the deflection of the elevator with respect to the body-fixed x axis and the slope of the fuselage's neutral axis that occurs at the hinge point. Thus, due to the deflection of the structure, there is a change in the turn angle of the flow, which will affect elevator effectiveness. Because we are using a flat plate to approximate the control surface, the pressure will be determined by Prandtl–Meyer flow on one side of the plate and by oblique shock theory on the other side. The resultant force acts at the midchord of the control surface. The x and z body forces are

$$F_{x,cs} = -(p_{cs,\ell} - p_{cs,u}) \sin \delta_{cs} S_{cs} \tag{36}$$

$$F_{z,cs} = -(p_{cs,\ell} - p_{cs,u}) \cos \delta_{cs} S_{cs} \tag{37}$$

The pitching moment due to the deflection of the control surface is

$$M_{cs} = z_{cs} F_{x,cs} - x_{cs} F_{z,cs} \tag{38}$$

Once all of the forces and moments due to the aerodynamics have been determined, the resultant body forces and the moment are summed from the individual components.

The pitching moment is the sum of the forces acting on each component of the vehicle along with the pitching moment due to the engine thrust. From Fig. 1, it is readily apparent that the thrust force has an influence on the pitching moment, because it is located below the center of mass of the vehicle. The total moment acting on the vehicle is then

$$M = M_f + M_u + M_n + M_a + M_{cs} + M_{\text{inlet}} + z_{\mathcal{T}} \mathcal{T} \tag{39}$$

The forces F_x and F_z can be translated into the lift and drag acting on the aircraft by using the following coordinate transformation [15]:

$$\mathcal{R}_\alpha = \begin{bmatrix} \cos\alpha & 0 & \sin\alpha \\ 0 & 1 & 0 \\ -\sin\alpha & 0 & \cos\alpha \end{bmatrix} \tag{40}$$

The rotation matrix $\mathcal{R}_\alpha$ carries the body-axis frame to the stability axis by premultiplying a vector in the body-fixed frame by the rotation matrix $\mathcal{R}_\alpha$. The stability axis system is aligned such that its x axis is coincident with the velocity vector. The lift and drag are then defined in terms of the body forces as

$$L = F_x \sin\alpha - F_z \cos\alpha \tag{41}$$

$$D = -F_x \cos\alpha - F_z \sin\alpha \tag{42}$$

whereas the pitching moment remains invariant under the change of coordinates. Note in this case that F_x is positive forward, D is positive aft, F_z is positive down, and L is positive up.

III. Flexible Aircraft Model

For full-scale air-breathing hypersonic vehicles, flexibility effects play an important part in the aerodynamics of the aircraft. From the equations derived in the previous section, it is evident that the structural bending will manifest itself in the flow deflection angle and, as a result, will have an effect on the angle of the bow shock, thereby affecting the pressures downstream of the shock. For example, deflection of the forebody affects the thrust not only through changes in pressure due to the moving shock, but also through the effects of mass flow spillage in the event that a movable cowl door does not have sufficient bandwidth to track the high-frequency movements of the bow shock. It is likely that a moveable cowl door would, in reality, be scheduled as a function of Mach and angle of attack. Thus, one can expect that structural vibrations will cause the engine to operate under off-design conditions much of the time, because of the effects of the forebody shock on inlet pressure and mass flow spillage.

A. Vibrational Model

For the dynamic simulation, a vibrational model of the fuselage is necessary. Hypersonic vehicles are generally tapered at the fore and aft ends, thus concentrating the mass toward the middle of the vehicle. In this case, one would expect the deflection of the fuselage at the center of mass to be much less than that at either end of the vehicle. Therefore, we model the fuselage as comprising two cantilever beams, one pointing forward and one pointing aft, and each has one end clamped at the center of mass of the fuselage. Thus, the root of each beam will rotate and translate according to the motion of the aircraft's center of mass. Only the transverse displacements of the beams are of interest, and it is assumed that the displacements are sufficiently small such that Hooke's law is valid. We will denote the displacement and rotation of the beams with subscripts f and a. The coordinate system of the double-cantilever beam system is given in Fig. 9. At the center of gravity, there will be no *structural displacement or rotation* of the beams, due to the assumption that they are clamped at this point. The coordinate x is measured positive from the front of the vehicle toward the back. The forward beam has a length of $\bar{x}$ to indicate the location of the center of mass. The length of the aft pointing beam is $L_a = L - \bar{x}$.

It can be shown [16] that the transverse vibration of a cantilever beam with constant EI and constant mass density $\hat{m}$ satisfies the following partial-differential equation:

$$EI \frac{\partial^4 w(x,t)}{\partial x^4} + \hat{m} \frac{\partial^2 w(x,t)}{\partial t^2} = 0 \tag{43}$$

Assuming that the solution is of the form $w(x,t) = \phi(x) f(t)$, then Eq. (43) can be separated into two ordinary differential equations:

$$EI \frac{d^4 \phi(x)}{\mathrm{d}x^4} - \omega^2 \hat{m} \phi(x) = 0 \tag{44}$$

$$\frac{d^2 f(t)}{\mathrm{d}t^2} + \omega^2 f(t) = 0 \tag{45}$$

Defining $\beta^4 = \omega^2 \hat{m}/(EI)$, Eq. (44) takes the form

$$\frac{d^4 \phi(x)}{\mathrm{d}x^4} - \beta^4 \phi(x) = 0 \tag{46}$$

The solution to Eq. (46) is

$$\phi(x) = A \sin \beta x + B \cos \beta x + C \sinh \beta x + D \cosh \beta x \tag{47}$$

For the forward-facing beam, we apply the following boundary conditions, where $x = \bar{x}$ is the root and $x = 0$ is the front tip:

$$\phi_f(\bar{x}) = 0 \tag{48}$$

$$\phi_f'(\bar{x}) = 0 \tag{49}$$

$$\phi_f''(0) = 0 \tag{50}$$

$$\phi_f'''(0) = 0 \tag{51}$$

and we obtain the following frequency equation

$$\cos \beta\bar{x} \cosh \beta\bar{x} = -1 \tag{52}$$

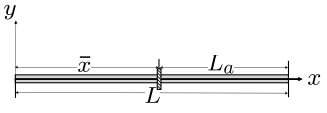

Fig. 9 Beam coordinate system definition.

Equation (52) has an infinite number of solutions β_k that can only be found through the application of numerical methods. The mode shapes for the forward beam corresponding to the frequencies can be shown to be

$$\phi_{f,k}(x) = A_{f,k}[(\sin\beta_{f,k}\bar{x} - \sinh\beta_{f,k}\bar{x})(\sin\beta_{f,k}x + \sinh\beta_{f,k}x) + (\cos\beta_{f,k}\bar{x} + \cosh\beta_{f,k}\bar{x})(\cos\beta_{f,k}x + \cosh\beta_{f,k}x)] \tag{53}$$

The mode shapes $\phi_{f,k}(x)$ form an orthogonal set of solutions and we choose the value of $A_{f,k}$ such that the mode shapes are mass-normalized:

$$\int_0^{\bar{x}} \hat{m}\phi_{f,j}(x)\phi_{f,k}(x)\,\mathrm{d}x = \begin{cases} 0 & \text{if } j \neq k \\ 1 & \text{if } j = k \end{cases} \tag{54}$$

For the aft beam, the derivation for the resulting frequency equation and mode shapes parallels that of the forward-facing beam and, therefore, is not included here. The interested reader is referred to [17] for more details.

The displacement and slope of the structure, determined from the mode shapes for the fore and aft beams, are shown in Fig. 10

B. Forced Response

For the case where there are distributed and concentrated loads on the beam, Eq. (43) becomes

$$EI\frac{\partial^4 w(x,t)}{\partial x^4} + \hat{m}\frac{\partial^2 w(x,t)}{\partial t^2} = p(x,t) + P_j(t)\delta(x - x_j) \tag{55}$$

From the expansion theorem, the solution of Eq. (55) is

$$w(x,t) = \sum_{k=1}^{\infty} \phi_k(x)\eta_k(t) \tag{56}$$

It can be shown that $\eta_k(t)$ satisfies the differential equation [18]

$$\ddot{\eta}_k + \omega_k^2\eta_k = N_k(t) \tag{57}$$

where the generalized modal force associated with the kth mode shape is

$$N_k(t) = \int_0^L \phi_k(x)p(x,t)\,\mathrm{d}x + \sum_{j=1}^{l} \phi_k(x_j)P_j(t) \tag{58}$$

In Eq. (58), l is the number of concentrated forces applied to the beam. We will require Eq. (58) when we derive the equations of motion for the flexible aircraft in the next section.

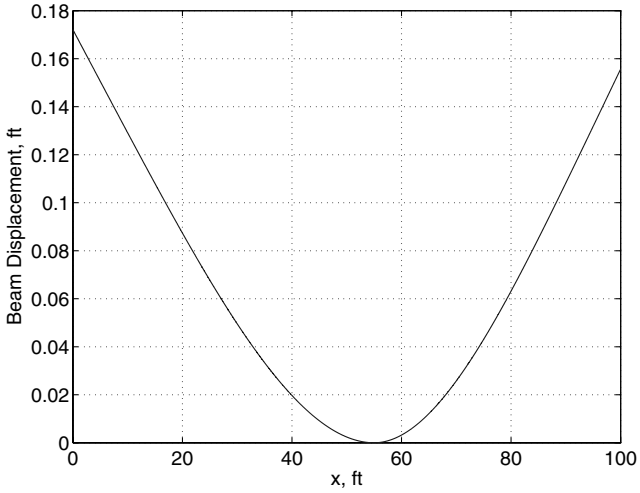

a) Fuselage displacement

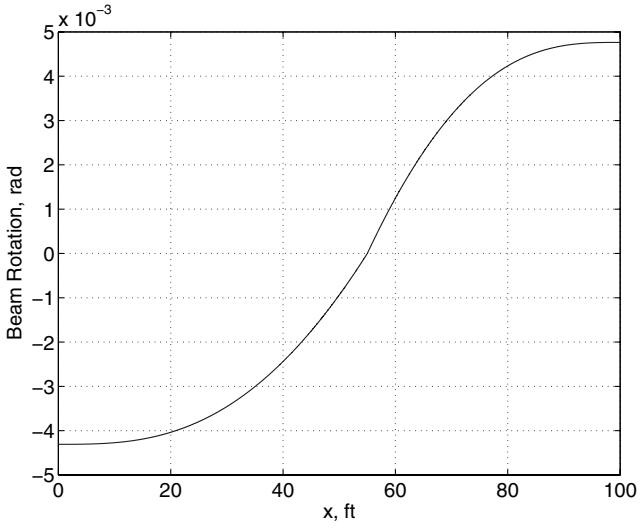

b) Fuselage rotation

Fig. 10 First bending mode.

IV. Lagrange's Equations for a Flexible Aircraft

There are several approaches in the literature that discuss the determination of the equations of motion for a flexible aircraft. Bisplinghoff et al. [19] derive the equations of motion for an "unconstrained vehicle" and show that the rigid body and the vibrational mode shapes are orthogonal. Waszak and Schmidt [20], use a "mean elastic axis" that physically decouples the rigid-body equations and the equations of motion that describe the vibration of the aircraft. In both the Waszak and Bisplinghoff models, the coupling of the rigid-body rotation and translation with the structural modes is implicit, as the effects of the bending are only present in the forces and moments. This means that the mean axis assumption does not capture any inertial coupling that may be present between the aircraft's pitch acceleration, the aircraft's normal acceleration, and the transverse vibration of the aircraft. Papers by Olsen [21] and Buttrill, et al. [22] each take into account the coupling between the aircraft's linear and angular accelerations with the elastic modes. Olsen makes no assumption on how the mode shapes are represented,, whereas Buttrill assumes a lumped-mass approach. Finally, Meirovitch and Tuzcu [23] give another approach that attempts to unify the disciplines of dynamics, controls, aeroelasticity, and aerodynamics. Meirovitch gives a rather lengthy argument against the use of mean elastic axes and for the need to ensure that the rigid-body and elastic-mode coupling is present. Meirovitch then presents a derivation of the equations of motion for an elastic aircraft based upon Lagrange's equations and the use of quasi-coordinates. The preceding approaches all seek to achieve a realistic model that captures the coupling between the aircraft rigid-body dynamics and the structural dynamics of the vehicle. Our approach (see Bolender and Doman [17]) is to assume no specific structural model a priori to the derivation of the equations of motion. The derivation that is presented in [17] assumes that there are no torsional vibrations, no longitudinal or "pogo" vibrations, and that the mass of the aircraft is constant. To derive the equations of motion for this system, we used Lagrange's equations. Recall that the Lagrangian is defined as $\mathcal{L} = \mathcal{J} - \mathcal{V}$. If we assume that there are n generalized coordinates q_i, then Lagrange's equations are

$$\frac{\mathrm{d}}{\mathrm{d}t}\frac{\partial \mathcal{L}}{\partial \dot{q}_i} - \frac{\partial \mathcal{L}}{\partial q_i} = Q_i, \qquad i = 1, \ldots, n \tag{59}$$

where Q_i is the generalized force associated with generalized coordinate q_i. The generalized force can be either a force or moment, depending upon whether the generalize coordinate q_i represents a translation or rotation. The generalized forces are determined from

the following equation for the virtual work, due to nonconservative forces:

$$\delta \mathcal{W} = \sum_{i=1}^{n} Q_i \delta q_i \tag{60}$$

Alternatively, the ith generalized force can be determined from

$$Q_i = \sum_{i=1}^{N} \boldsymbol{f}_i \cdot \partial \boldsymbol{r} / \partial q_r$$

where $\boldsymbol{f}_i$ is the ith applied nonconservative force and N is the number of nonconservative forces applied to the body.

The derivation of the potential and kinetic energies for a flexible vehicle is quite detailed and, for brevity, it is omitted here. However, the reader is referred to Bolender and Doman [17] for the full derivation. Under the assumptions that flight occurs only in the longitudinal plane and that the vehicle has infinite lateral stiffness, the kinetic energy of a flexible aircraft simplifies to

$$\begin{aligned}\mathcal{J} =& \frac{1}{2} m \dot{\boldsymbol{r}}_0 \cdot \dot{\boldsymbol{r}}_0 + \frac{1}{2} \boldsymbol{\omega} \cdot I \boldsymbol{\omega} + \frac{1}{2} \sum_{i=1}^{\infty} \dot{\eta}_{z,i}^2 + \frac{1}{2} P^2 \sum_{i=1}^{\infty} \eta_{z,i}^2 \\ &+ \frac{1}{2} Q^2 \sum_{i=1}^{\infty} \eta_{z,i}^2 + (\dot{\boldsymbol{r}}_0 \times \boldsymbol{\omega}) \cdot \sum_{i=1}^{\infty} \lambda_{z,i} \eta_{z,i} \boldsymbol{e}_3 + \dot{\boldsymbol{r}}_0 \cdot \left(\sum_{i=1}^{\infty} \lambda_{z,i} \dot{\eta}_{z,i} \boldsymbol{e}_3 \right) \\ &+ Q^2 \sum_{i=1}^{\infty} \sigma_{z,i} \eta_{z,i} - Q \sum_{i=1}^{\infty} \psi_{xz,i} \dot{\eta}_{z,i}\end{aligned} \tag{61}$$

where

$$\sigma_{z,i} \triangleq \int_B w \phi_{z,i}(u, v, w)\, \mathrm{d}m \tag{62}$$

$$\lambda_{z,i} \triangleq \int_B \phi_{z,i}(u, v, w)\, \mathrm{d}m \tag{63}$$

$$\psi_{xz,i} \triangleq \int_B u \phi_{z,i}(u, v, w)\, \mathrm{d}m \tag{64}$$

The potential energy is given by

$$\mathcal{V} = -m \boldsymbol{g} \cdot \boldsymbol{r}_0 + \frac{1}{2} \sum_{i=1}^{\infty} \omega_{z,i}^2 \eta_{z,i}^2 \tag{65}$$

Now we want to address the derivation of the equations of motion for the longitudinal dynamics of a flexible aircraft. The structural model is assumed to consist of two cantilever beams fixed at the origin. One reason for choosing this particular structural model was due to the fact that there was no available finite-element model of the vehicle structure. In addition, this particular choice for the elastic structure exhibits coupling between the pitch attitude and the normal acceleration with the elastic modes. The first beam will point toward the nose of the vehicle and the second will point toward the tail. Each beam will be assumed to deflect only in the z body-axis direction, and the length of each beam will be assumed to be much larger than the thickness (i.e., we neglect any rotatory inertia effects). Furthermore, the deflections are assumed to be small enough such that Hooke's law is valid.

The inertial frame (see Fig. 11) will be denoted by the unit vector triad $(\boldsymbol{n}_1, \boldsymbol{n}_2, \boldsymbol{n}_3)$, and the body-axes frame unit vectors will be denoted by $(\boldsymbol{e}_1, \boldsymbol{e}_2, \boldsymbol{e}_3)$. The inertial frame is oriented such that $\boldsymbol{n}_1$ points north, $\boldsymbol{n}_2$ points east, and $\boldsymbol{n}_3 = \boldsymbol{n}_1 \times \boldsymbol{n}_2$ is positive down. The body axes are oriented in the vehicle with $\boldsymbol{e}_1$ positive out the nose and $\boldsymbol{e}_2$ positive out the right wing. The unit vector $\boldsymbol{e}_3 = \boldsymbol{e}_1 \times \boldsymbol{e}_2$ is positive out the bottom of the aircraft. Both sets of unit vectors form orthogonal triads.

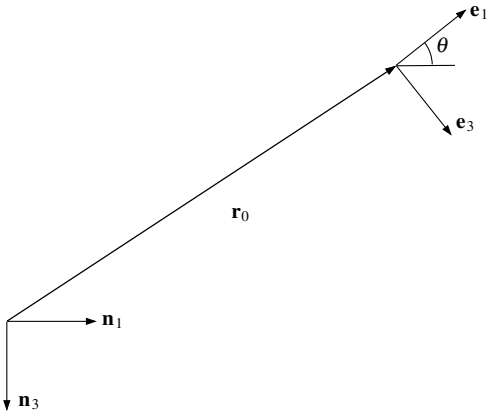

Fig. 11 Inertial and body-fixed reference frames.

It is also assumed that the aircraft is flying with wings level (no roll) and without sideslip, and so the longitudinal and lateral directional equations decouple. The $\boldsymbol{n}$ frame is carried into the $\boldsymbol{e}$ frame by the coordinate transformation:

$$\mathcal{R}_\theta = \begin{bmatrix} \cos\theta & 0 & -\sin\theta \\ 0 & 1 & 0 \\ \sin\theta & 0 & \cos\theta \end{bmatrix} \tag{66}$$

such that $\boldsymbol{e} = \mathcal{R}_\theta \boldsymbol{n}$. The angular velocity of the aircraft is $\boldsymbol{\omega} = Q\boldsymbol{e} = \dot{\theta}\boldsymbol{n}_2$. From the definition of $\mathcal{R}_\theta$, it is evident that $Q = \dot{\theta}$.

The position of the center of mass is given in the $\boldsymbol{n}$ frame as $\boldsymbol{r}_0 = X\boldsymbol{n}_1 + Z\boldsymbol{n}_3$ and in the $\boldsymbol{e}$ frame as:

$$\boldsymbol{r}_0 = x\boldsymbol{e}_1 + z\boldsymbol{e}_2 = (X\cos\theta - Z\sin\theta)\boldsymbol{e}_1 + (X\sin\theta + Z\cos\theta)\boldsymbol{e}_2$$

The velocity of the center of mass in the $\boldsymbol{e}$ frame is

$$\dot{\boldsymbol{r}}_0 = \delta \boldsymbol{r}_{P/0}/\delta t + \boldsymbol{\omega} \times \boldsymbol{r}_{P/0} = (\dot{x} + Qz)\boldsymbol{e}_1 + (\dot{z} - Qx)\boldsymbol{e}_2 = U\boldsymbol{e}_1 + W\boldsymbol{e}_2$$

For the elastic modes of the aircraft, we are only interested in the first fuselage bending mode. The elastic deformation of the fuselage is modeled by two cantilever beams that are fixed at the center of mass such that they have no rotation or displacement relative to the center of mass. It is assumed that the height of the beam is negligible as compared with the length so that $\boldsymbol{\rho} = u\boldsymbol{e}_1$ and $\boldsymbol{d} = \mathrm{d}\boldsymbol{e}_3$. We denote the modal coordinates of the forward and aft beams as η_f and η_a, respectively. The displacement of each beam can be written as

$$d_f = \sum_{i=1}^{\infty} \phi_{f,i} \eta_{f,i}$$

and

$$d_a = \sum_{i=1}^{\infty} \phi_{a,i} \eta_{a,i}$$

We can now write the kinetic energy of the aircraft using Eq. (61):

$$\begin{aligned}\mathcal{J} =& \tfrac{1}{2} m[(\dot{x} + Qz)^2 + (\dot{z} - Qx)^2] + \tfrac{1}{2} I_{yy} Q^2 + \tfrac{1}{2}\dot{\eta}_a^2 + \tfrac{1}{2}\dot{\eta}_f^2 \\ &+ \tfrac{1}{2} Q^2 \left(\eta_a^2 + \eta_f^2 \right) + (\dot{\boldsymbol{r}}_0 \times \boldsymbol{\omega}) \cdot (\lambda_a \eta_a + \lambda_f \eta_f)\boldsymbol{e}_3 + \dot{\boldsymbol{r}}_0 \cdot (\lambda_a \dot{\eta}_a \\ &+ \lambda_f \dot{\eta}_f)\boldsymbol{e}_3 + Q^2(\sigma_f \eta_f + \sigma_a \eta_a) - Q(\psi_f \dot{\eta}_f + \psi_a \dot{\eta}_a)\end{aligned} \tag{67}$$

Making the substitution for $\dot{\boldsymbol{r}}_0$, noting that

$$\dot{\boldsymbol{r}}_0 \times \boldsymbol{\omega} = -Q(\dot{z} - Qx)\boldsymbol{e}_1 + Q(\dot{x} + Qz)\boldsymbol{e}_3$$

and using the assumption that, because $w \ll L$, $w \approx 0 \Rightarrow \sigma \approx 0$ simplifies the kinetic energy to

$$\mathcal{J} = \tfrac{1}{2}m[(\dot{x} + Qz)^2 + (\dot{z} - Qx)^2)] + \tfrac{1}{2}I_{yy}Q^2 + \tfrac{1}{2}\dot{\eta}_a^2 + \tfrac{1}{2}\dot{\eta}_f^2 + \tfrac{1}{2}Q^2\left(\eta_a^2 + \eta_f^2\right) + Q(\dot{x} + Qz)(\lambda_a\eta_a + \lambda_f\eta_f) + (\dot{z} - Qx)(\lambda_a\dot{\eta}_a + \lambda_f\dot{\eta}_f) - Q(\psi_f\dot{\eta}_f + \psi_a\dot{\eta}_a) \tag{68}$$

To determine the potential energy, we write the gravity in the body-axes coordinate system using the rotation matrix R_θ:

$$\boldsymbol{g} = g\boldsymbol{n}_3 \tag{69}$$

$$= g(-\sin\theta\boldsymbol{e}_1 + \cos\theta\boldsymbol{e}_3) \tag{70}$$

For the strain energy, we again are only using the fundamental mode shape. It can be shown that the strain energy is

$$\mathcal{V}_s = \tfrac{1}{2}\left(\omega_f^2\eta_f^2 + \omega_a^2\eta_a^2\right) \tag{71}$$

Thus, the total potential is

$$\mathcal{V} = -mg(-x\sin\theta + z\cos\theta) + \tfrac{1}{2}\left(\omega_f^2\eta_f^2 + \omega_a^2\eta_a^2\right) \tag{72}$$

The Lagrangian for the flexible aircraft is then

$$\mathcal{L} = \mathcal{J} - \mathcal{V} = \tfrac{1}{2}m[(\dot{x} + Qz)^2 + (\dot{z} - Qx)^2] + \tfrac{1}{2}I_{yy}Q^2 + \tfrac{1}{2}\dot{\eta}_a^2 + \tfrac{1}{2}\dot{\eta}_f^2 + \tfrac{1}{2}Q^2\left(\eta_a^2 + \eta_f^2\right) + Q(\dot{x} + Qz)(\lambda_a\eta_a + \lambda_f\eta_f) + (\dot{z} - Qx)(\lambda_a\dot{\eta}_a + \lambda_f\dot{\eta}_f) - Q(\psi_f\dot{\eta}_f + \psi_a\dot{\eta}_a) + mg(-x\sin\theta + z\cos\theta) - \tfrac{1}{2}\left(\omega_f^2\eta_f^2 + \omega_a^2\eta_a^2\right) \tag{73}$$

Before proceeding with Lagrange's equations, the virtual work needs to be determined. It is assumed that the aerodynamic and propulsive forces acting on the aircraft (lift, drag, and thrust) are resolved into their body-axes forces such that the forces acting on the aircraft are F_x in the $\boldsymbol{e}_1$ direction and F_z in the $\boldsymbol{e}_3$ direction. The moment about the origin of the inertial triad is $M + zF_x - xF_x$. For the elastic modes, the modal forces due to the aerodynamics are given by

$$N_f = \int_f p_f(u,t)\phi_f(u)\,\mathrm{d}u + \sum_{j=1}^{n}\phi_f(u_j)P_{f,j}(t) \tag{74}$$

$$N_a = \int_a p_a(u,t)\phi_a(u)\,\mathrm{d}u + \sum_{j=1}^{n}\phi_a(u_j)P_{a,j}(t) \tag{75}$$

For this aircraft, a concentrated load occurs on the aft beam where the elevon attaches to the beam. The hinge point of the elevon rotates and translates with the beam at this location. Thus, the forces and moments produced by the elevon are affected by the structural bending. To include the effects of damping, we assume that the damping force is proportional to the modal velocities $\dot{\eta}_f$ and $\dot{\eta}_a$ and is given as $2\zeta\omega\dot{\eta}$. The virtual work in the body-axis frame is

$$\delta\mathcal{W} = F_x\delta x + F_z\delta z + (M + zF_x - xF_z)\delta\theta + (-2\zeta\omega_f\dot{\eta}_f + N_f)\delta\eta_f + (-2\zeta\omega_a\dot{\eta}_a + N_a)\delta\eta_a \tag{76}$$

The generalized coordinates are x, z, θ, η_f, and η_a. Applying Lagrange's equations and using the definitions $U \triangleq \dot{x} + Qz$ and $W \triangleq \dot{z} - Qx$, we obtain the following set of differential equations that completely describe the motion of a flexible vehicle whose structural dynamics are modeled as two cantilever beams clamped at the center of gravity:

$$m\dot{U} + mQW + mg\sin\theta + \dot{Q}(\lambda_a\eta_a + \lambda_f\eta_f) + 2Q(\lambda_a\dot{\eta}_a + \lambda_f\dot{\eta}_f) = F_x \tag{77}$$

$$m\dot{W} - mQU - mg\cos\theta + \lambda_a\ddot{\eta}_a + \lambda_f\ddot{\eta}_f - Q^2(\lambda_a\eta_a + \lambda_f\eta_f) = F_z \tag{78}$$

$$\left(I_{yy} + \eta_a^2 + \eta_f^2\right)\dot{Q} + (\dot{U} + QW)(\lambda_a\eta_a + \lambda_f\eta_f) + 2Q(\eta_a\dot{\eta}_a + \eta_f\dot{\eta}_f) - \psi_a\ddot{\eta}_a - \psi_f\ddot{\eta}_f = M \tag{79}$$

$$\ddot{\eta}_f + (\dot{W} - QU)\lambda_f - \dot{Q}\psi_f + 2\zeta\omega_f\dot{\eta}_f + \left(\omega_f^2 - Q^2\right)\eta_f = N_f \tag{80}$$

$$\ddot{\eta}_a + (\dot{W} - QU)\lambda_a - \dot{Q}\psi_a + 2\zeta\omega_a\dot{\eta}_a + \left(\omega_a^2 - Q^2\right)\eta_a = N_a \tag{81}$$

In addition, we have two kinematic differential equations, one each for the downrange and altitude:

$$\dot{X} = U\cos\theta + W\sin\theta \tag{82}$$

$$\dot{h} = U\sin\theta - W\cos\theta \tag{83}$$

At this point, it is interesting to note the presence of the parameters ψ_a, ψ_f, λ_a, and λ_f in the equations of motion. These terms appear because of our choice of model for the structural dynamics. Recall that the structure we chose is constrained at the center of gravity and therefore rotates and translates according to the motion of the center of gravity. As a result, the rigid-body modes are capable of directly exciting the structural dynamics. Therefore, the rigid-body modes and the flexible modes are inertially coupled. In other words, the rigid-body rotation and translational modes are *not* orthogonal to the flexible modes. It is also worth noting that, if one assumes an infinitely rigid structure such that

$$\eta_f = \eta_a = \dot{\eta}_f = \dot{\eta}_a = \ddot{\eta}_f = \ddot{\eta}_a = 0$$

we recover the body-axis equations of motion for a rigid aircraft.

Another interesting consideration is to examine what occurs when one chooses a structural model that is not constrained at the center of gravity. This model appears to be more prevalent in the literature [19,20,24]. In the case of an unconstrained vehicle, the flexible modes become orthogonal to the rigid-body modes and, as a result, the inertial coupling terms vanish. When this occurs, one is left with a set of equations for the traditional rigid-body motion ($\dot{U}$, $\dot{W}$, $\dot{Q}$), and a set for the flexible modes. The equations of motion remain coupled, but they are coupled through the forces and moments, because the forces and moments still remain functions of the structural displacement.

From the preceding analysis, it is clear that the presence of inertial coupling in the equations of motion [Eqs. (77–81)] is obviously dependent upon the model chosen to represent the structural dynamics of the fuselage. Obviously, the presence of inertial coupling results in a system that is more complex and more difficult to control. The question of whether inertial coupling between the rigid-body states and the flexible states is necessary to properly capture the dynamics remains an open question.

A. Stability Axis Equations of Motion

Because the aerodynamic forces are written in terms of the lift and drag acting on the vehicle, it is advantageous to rewrite the body-axes equations of motion in terms of the stability axes. The transformation

matrix $\mathcal{R}_\alpha$, defined in the previous section, that carries the body axes to the stability axes and the following definitions

$$\tan\alpha \triangleq W/U$$

$$V_T^2 \triangleq U^2 + W^2$$

$$\dot{V}_T = (U\dot{U} + W\dot{W})/V_T$$

and

$$\dot{\alpha} = (U\dot{W} - W\dot{U})/(U^2 + W^2)$$

are used to obtain the stability axis equations of motion. The stability axis equations of motion are omitted due to their complexity, but they can be obtained using any available software package capable of performing symbolic mathematics.

V. Modal Analysis

To study the open-loop dynamics, the vehicle was trimmed in level flight at Mach 8 and altitude of 85,000 ft, then subsequently linearized about this trim condition. The vehicle geometry and mass properties are as given in Appendix A. The following results assume that LH2 is used as the fuel. The open-loop poles of the linearized dynamics are given in Table 2. The aircraft has an unstable short-period mode that can be attributed partly to the aft location of the center of gravity (assumed to be at 55% of the length of the vehicle). However, the lower forebody pressure and the thrust provide a nose-up pitching that is countered by the aft pressure resulting from the expansion of the scramjet exhaust and the upper-surface pressure, resulting in a positive M_α. If we consider the classical short-period approximation for a rigid vehicle, we gain further insight into the stability derivatives that influence the short-period pole locations. The characteristic equation for the short-period dynamics is

$$\Delta_{\text{sp}} = (V_t - Z_{\dot{\alpha}})s^2 - [Z_\alpha + (V_t - Z_{\dot{\alpha}})M_q + (V_t + Z_q)M_{\dot{\alpha}}]s + M_q Z_\alpha - (V_t + Z_q)M_\alpha \tag{84}$$

However, we can assume that $M_{\dot{\alpha}}$, $Z_{\dot{\alpha}}$, and Z_q are negligible when compared with the remaining terms, which leaves us with

$$\Delta_{\text{sp}} = V_t s^2 - (Z_\alpha + V_t M_q)s + M_q Z_\alpha - V_t M_\alpha \tag{85}$$

The roots of this equation are

$$s = \frac{Z_\alpha}{2V_t} \pm \frac{\sqrt{(Z_\alpha - V_t M_q)^2 + 4V_t^2 M_\alpha}}{2V_t} \tag{86}$$

Note that in the radicand of Eq. (86), the dominant term is $V_t^2(M_q^2 + M_\alpha)$, due to the high velocity of the aircraft. If $4M_\alpha + M_q^2 > 0$ then we will have unstable short-period dynamics. At high velocities, if we can neglect the pitch damping term M_q, a first approximation for the short-period frequency when $M_\alpha > 0$ is

$$s = Z_\alpha/(2V_t) \pm \sqrt{M_\alpha}$$

Table 2 Eigenvalues of linearized system: vehicle geometry, as given in Appendix A

Eigenvalue	Damping ratio	Natural freq., rad/s	Mode
$-2.72 \pm 49.3j$	0.055	49.4	Aeroelastic
$-0.376 \pm 16.2j$	0.0196	18.0	Flex
-1.42	1.00	1.42	Short-period
1.35	-1.00	1.35	Short-period
-5.79×10^{-4}	1.00	5.79×10^{-4}	Altitude
$-1.68 \times 10^{-5} \pm 0.0266j$	-6.31×10^{-4}	0.0266	Phugoid

The phugoid mode at this flight condition is stable and very lightly damped. Sachs [25] has shown the frequency of the phugoid is dependent upon the density gradient of the atmosphere and that the phugoid frequency is approximately $\sqrt{-g/h_s}$, where h_s is the scale height. In addition, there is an altitude mode present that one typically neglects for conventional aircraft. The altitude mode arises because of the force and moment dependency on the altitude and is primarily caused by the density lapse rate. Typically, this mode has a very low frequency, and in our case, this is indeed what occurs.

The final two modes that are present are the structural modes. These two modes comprise two stable complex-conjugate pairs of poles. The first pair of complex-conjugate poles has a natural frequency that is approximately the same as the frequency of the beams. The second pair of poles is at a much higher frequency and, in fact, is greater than the sum of the frequencies of the fore and aft beams. These two high-frequency poles appear to be an aeroelastic mode of the aircraft, as an analysis of the eigenvectors tells us that the most significant contributions are due to $\dot{\eta}_a$ followed by $\dot{\eta}_f$, with minor influences due to the airspeed and the pitch rate. For the pair of lower-frequency eigenvalues, the eigenvector is dominated by $\dot{\eta}_f$ then $\dot{\eta}_a$. Finally, the eigenvectors for the short-period mode exhibit the expected contributions from α and Q, but there are even larger contributions from both η and $\dot{\eta}$, highlighting the inertial coupling between normal acceleration, pitch rate, and the aeroelastic modes of the aircraft.

The poles and zeros are shown in Fig. 12 for a 2×2 system where the inputs are the elevator deflection and the equivalence ratio, and the outputs are the aircraft velocity and the flight-path angle $\gamma = \theta - \alpha$. Note that there are two pairs of complex–conjugate transmission zeros that are mirror images about the $j\omega$ axis. These zero pairs are associated with the flexible mode of the aircraft. The two real zeros seen in Fig. 12 that are a mirror image about the imaginary axis arise because of the flight-path angle dynamics. To command an increase in flight-path angle requires that the elevator deflect the trailing edge up, to create a nose-up pitching moment. Deflecting the elevator trailing edge up will instantaneously reduce the lift on the tail and the total lift on the vehicle, causing an initial drop in the flight-path angle and the altitude. The impact of this low-frequency right-half plane transmission zero is that it will severely restrict the bandwidth of any flight control system. Practically, this means that high-gain tracking tasks cannot be accomplished at this flight condition, due to the control system bandwidth limitations imposed by the right-half plane transmission zero. This suggests that configuration changes may be in order to change the location of the troublesome zero, to make the vehicle more amenable to feedback control. Clearly, feedback control will be necessary because the vehicle is open-loop unstable. However, feedback gains must be limited because of the right-half plane zero.

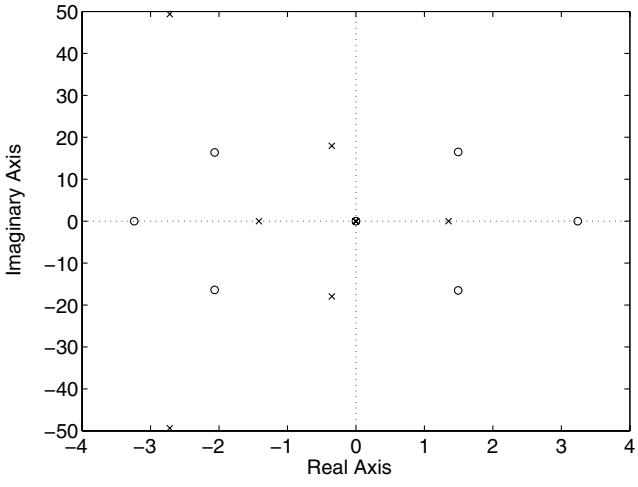

Fig. 12 Poles and transmission zeros of the linearized system.

Table 3 Eigenvalues of linearized system from [3]

Eigenvalue	Mode
$-0.55 \pm 16.46j$	First flex mode
-2.5	Short-period
2.31	Short-period
1.14×10^{-6}	Altitude
$-0.002 \pm 0.057j$	Phugoid

Table 4 Eigenvalues of linearized system for the geometry given in [3]

Eigenvalue	Mode
202	Aeroelastic
-148	Aeroelastic
$-4.23 \times 10^{-1} \pm 20.7j$	First flex mode
-2.48	Short-period
2.40	Short-period
-9.24×10^{-4}	Altitude
$-3.36 \times 10^{-5} \pm 0.021$	Phugoid

A. Comparison of Modeling Approaches to Chavez–Schmidt Configuration

Next, we compare the system poles for the configuration given in Chavez and Schmidt [3] using their modeling approach for the aerodynamics, propulsion system, and structural dynamics with ours. The linearized flight dynamics as given in [3] are at Mach 8 and an altitude of 85,000 ft. The results are given in Tables 3 and 4. The results in Table 4 assume that there is no cowl door present, but mass flow spillage effects on the thrust are modeled.

Note that the primary difference between the linearized dynamics is the presence of an aeroelastic mode using the double-cantilever structural model. This mode is very unstable with a pole located at 202 rad/s. The two models give very comparable results for the short-period dynamics. Note there are sign and frequency differences in the phugoid and altitude modes. These are not dominant modes due to their large time constants, but the differences in the pole locations can be attributed to differences used to compute the aerodynamics. The difference in the frequency of the flexible mode is somewhat unexpected, but probably can be made to match better with the appropriate choice of EI for the beams. The results from [3] do not have an aeroelastic mode because of the difference in the structural models. The aeroelastic model in [3] is a lumped-mass model that was based on a finite-element analysis of a conceptual design for an air-breathing hypersonic vehicle. It is worth noting that for this particular model, a mean axis approximation was employed, and so the rigid-body modes are decoupled inertially from the flexible modes. However, it appears that the additional modeling fidelity developed here has produced similar results as the approach given in Chavez and Schmidt [3]. With a different model for the fuselage vibration (i.e., one that is based on the dynamics of a structure that is not constrained at any interior point), the structural dynamics can modified to be more in line with that given in [3].

VI. Conclusions

A nonlinear model of the aerodynamics, propulsion system, and structural dynamics for a representative air-breathing hypersonic vehicle has been presented. The model was derived from first principles and captures the interaction between the propulsion system, the aerodynamics, and the structural dynamics. The equations of motion for the flexible aircraft were derived using Lagrange's equations and include the effects of pitch acceleration and normal acceleration on the structural modes. We show that, for the particular structural model used in the analysis, significant inertial coupling of the rigid-body and structural modes occurs.

We investigated the effects of mass flow on the system dynamics. It had been postulated that perturbations in the flow turning angle due to flexing of the fuselage under aerodynamic loads and perturbations in the angle of attack could adversely affect the position of the bow shock. The change in the bow shock angle relative to the freestream would then cause the thrust, lift, and pitching moment to vary due to increased spillage of mass flow. It was found that as the flow turn angle increases due to increasing angle of attack, the amount of mass flow spilled does indeed increase. However, there is also a corresponding increase in captured mass flow. Further analysis showed that there was little sensitivity to the thrust due to varying angle of attack, especially as the fuel equivalence ratio was increased. The poles and transmission zeros were also found to be insensitive to a perturbation in flow deflection angle, which means that the effects are practically negligible for the purposes of closed-loop control design.

For this particular aircraft geometry, the linearized aircraft model has unstable short-period and phugoid modes. The short-period mode is dominated by the M_α term, which for this aircraft is positive, resulting in a pair of unstable, real poles. There are also two additional structural modes. The first mode has a frequency that is close to the natural frequency of the first bending mode. The second mode is at a frequency that is approximately 275% higher than the beam frequency, and this mode exhibits significant coupling between the velocity, pitch rate, and the modal velocities of the two cantilever beams that are used to model the structural dynamics. We also showed that the aircraft model indicates that the flight control system performance is limited due to the presence of a low-frequency right-half plane transmission zero in the elevator, throttle to velocity, flight-path angle transfer matrix. Although this zero is present on any aircraft with a horizontal tail, the magnitude of the right-half plane zero is typically large enough that it does not restrict the bandwidth of the closed-loop control system. Research into the design parameters that cause this right-half plane transmission zero to be close to the origin is ongoing.

Finally, we compared of the poles of a reference configuration whose aerodynamics and structural dynamics were modeled using the approach described in this paper to an approach found in the literature. We found that the "classical" longitudinal aircraft dynamics (short-period, phugoid, and altitude modes) were very similar. The only discrepancy arose in the structural dynamics, and the differences are attributed to the two very different aeroelastic models that were used in the analysis.

Appendix A: Vehicle Geometry and Mass Properties

Next is a list of the numerical values for the aircraft geometry. Note that all vertical and horizontal distances are referenced from the nose of the aircraft.

$$L = 100 \text{ ft} \qquad L_f = 47 \text{ ft} \qquad L_a = 33 \text{ ft} \qquad L_n = 20 \text{ ft}$$

$$\tau_{1,u} = 3 \text{ deg} \qquad \tau_{1,\ell} = 6.2 \text{ deg} \qquad \tau_2 = 14.41 \text{ deg}$$

$$x_{cs} = 85 \text{ ft} \qquad A_e = 5 \text{ ft}^2/\text{ft} \qquad A_n = 6.35 \qquad h_i = 3.5 \text{ ft}$$

$$\bar{x} = 55 \text{ ft} \qquad \bar{z} = 0 \text{ ft} \qquad S_e = 17 \text{ ft}^2/\text{ft} \qquad z_{cs} = 3.5 \text{ ft}$$

The mass properties of the vehicle are

$$I_{yy} = 5 \times 10^5 \text{ slugs} \cdot \text{ft}^2/\text{ft} \qquad m = 300 \text{ slugs/ft}$$

$$EI = 466350000 \text{ lb}_f \cdot \text{ft}^2/\text{ft} \qquad \hat{m}_f = 2.4545 \text{ slugs} \cdot \text{ft}^{-1}/\text{ft}$$

$$\hat{m}_a = 3.6667 \text{ slugs} \cdot \text{ft}^{-1}/\text{ft}$$

Acknowledgment

Part of this work was performed while the first author held a National Research Council Research Associateship Award at the Air Force Research Laboratory.

References

[1] Schmidt, D., "Dynamics and Control of Hypersonic Aeropropulsive/Aeroelastic Vehicles," AIAA Paper 92-4326, Aug. 1992.

[2] McRuer, D., "Design and Modeling Issues for Integrated Airframe/Propulsion Control of Hypersonic Flight Vehicles," *Proceedings of the 1992 American Control Conference*, American Automatic Control

Council, Evanston, IL, 1991, pp. 729–34.
[3] Chavez, F., and Schmidt, D., "Analytical Aeropropulsive/Aeroelastic Hypersonic-Vehicle Model with Dynamic Analysis," *Journal of Guidance, Control, and Dynamics*, Vol. 17, No. 6, Nov.–Dec. 1994, pp. 1308–1319.
[4] Schmidt, D., and Velapoldi, J., "Flight Dynamics and Feedback Guidance Issues for Hypersonic Air-breathing Vehicles," AIAA Paper 1999-4122, Aug. 1999.
[5] Von Eggers Rudd, L., and Pines, D., "Integrated Propulsion Effects on the Dynamic Stability and Control of Hypersonic Waveriders," AIAA Paper 2000-3826, July 2000.
[6] Shaughnessy, J., Pickney, S., McMinn, J., Cruz, C., and Kelley, M., "Hypersonic Vehicle Simulation Model: Winged-Cone Configuration," NASA Langley Research Center TM-102610, 1990.
[7] Haiges, K., Tich, E., and Madden, K., "Robust Control Law Development for Modern Aerospace Vehicles Task 1: Model Development," Northrup Grumman Aircraft Division, Interim Report WRDC-TR-89-3080, 1989.
[8] Anderson, J. D., *Hypersonic and High Temperature Gas Dynamics*, McGraw–Hill, New York, 1989.
[9] Anon., "Equations, Tables, and Charts for Compressible Flow," Ames Aeronautical Laboratory, Tech. Rep. NACA-1135, National Advisory Committee for Aeronautics, Moffett Field, CA, 1953.
[10] John, J., *Gas Dynamics*, Allyn and Bacon, Boston, 1984, Chap. 10, pp. 139–150.
[11] Heiser, W., and Pratt, D., *Hypersonic Airbreathing Propulsion*, AIAA, Washington, D.C., 1994, pp. 109–143.
[12] Bradford, J., and Olds, J., "Improvements and Enhancements to SCCREAM, A Conceptual RBCC Engine Analysis Tool," AIAA Paper 98-3775, 1998.
[13] Ikawa, H., "Rapid Methodology for Design and Performance Prediction of Integrated Supersonic Combustion Ramjet Engine," *Journal of Propulsion and Power*, Vol. 7, No. 3, 1991, pp. 437.
[14] Anon., *Handbook of Aviation Fuel Properties*, Coordinating Research Council, Atlanta, GA, 1983.
[15] Stevens, B., and Lewis, F., *Aircraft Control and Simulation*, Wiley-Interscience, New York, 1992, pp. 62–62.
[16] Meirovitch, L., *Analytical Methods in Vibrations*, MacMillan, New York, 1967, pp. 135–143, 161–163.
[17] Bolender, M., and Doman, D., "A Non-Linear Model for the Longitudinal Dynamics of a Hypersonic Air-breathing Vehicle," AIAA Paper 2005-6255, Aug. 2005.
[18] Meirovitch, L., *Analytical Methods in Vibrations*, MacMillan, New York, 1967, pp. 287–289.
[19] Bisplinghoff, R., Ashley, H., and Halfman, R., *Aeroelasticity*, Addison-Wesley, Reading, MA, 1955.
[20] Waszak, M., and Schmidt, D., "Flight Dynamics of Aeroelastic Vehicles," *Journal of Aircraft*, Vol. 25, No. 6, June 1988, pp. 563–571.
[21] Olsen, J. J., "Unified Flight Mechanics and Aeroelasticity for Accelerating, Maneuvering, Flexible Aircraft," *Structural Aspects of Flexible Aircraft Control* [CD ROM], NATO Research and Technology Organization, Applied Vehicle Technology Panel, Neuilly-sur-Seine, France, 1999.
[22] Buttrill, C., Zeiler, T., and Arbuckle, P., "Nonlinear Simulation of a Flexible Aircraft in Maneuvering Flight," AIAA Paper 87-2501, 1987, pp. 122–133.
[23] Meirovitch, L., and Tuzcu, I., "Integrated Approach to the Dynamics and Control of Flexible Manuevering Aircraft," NASA CR-2003-211748, June 2003.
[24] Milne, R., "Dynamics of the Deformable Airplane," Her Majesty's Stationary Office, Tech. Repts. and Memoranda 3345, Sept. 1964.
[25] Sachs, G., "Longitudinal Long-Term Modes in Super- and Hypersonic Flight," *Journal of Guidance, Control, and Dynamics*, Vol. 28, No. 3, May–June 2005, pp. 539–541.

P. Weinacht
Associate Editor